**Indonesian Journal of Electrical Engineering and Computer Science**
Vol. 42, No. 3, June 2026, pp. 865∼874
ISSN: 2502-4752, DOI: 10.11591/ijeecs.v42.i3.pp865-874 

# A computational framework for detection, classification, and visualization of magnetic nulls in multi-spacecraft observations

**Sri Ekawati[1,2], Dongsheng Cai[2,3], Hiroyuki Kudo[2]**
[1]Research Center for Climate and Atmosphere, National Research and Innovation Agency (BRIN), Bandung, Indonesia
[2]Department of Computer Science, University of Tsukuba, Tsukuba, Japan
[3]Nagoya University of Commerce and Business (NUCB), Nagoya, Japan

**Article Info**

***Article history:***

Received Oct 15, 2025
Revised Mar 17, 2026
Accepted May 26, 2026

***Keywords:***

Magnetic null detection
MMS mission
Topological classification
Computational pipeline
Plasma physics

**ABSTRACT**

Magnetic nulls, defined as locations where the magnetic field magnitude becomes zero, are theoretically well defined however practically difficult to locate, validate, and interpret. To address these challenges, this paper introduces a novel, modular, and fully reproducible automated framework for magnetic null detection, classification, and visualization based on multi-spacecraft observations. The proposed framework consists of two open-source modules: an automated data ingestion and null detection module, and a topological classification and three-dimensional visualization module. Magnetic nulls are detected by combining eigenvalue analysis of the magnetic field gradient tensor with tetrahedron-based geometric validation, enabling both numerical stability assessment and physical consistency checks. Meanwhile, detected nulls are classified into radial (Type A, B) and spiral (Type As, Bs) topologies, and their local magnetic structures are visualized through reconstructed three-dimensional magnetic field lines. The main contribution of this work is the tight integration of detection, numerical validation, classification, and visualization within a single end-to-end pipeline, ensuring consistency between computational output and physical interpretation. The framework is validated using four previously reported electron diffusion region (EDR) events and one storm-time substorm event. The detected null times closely agree with the reported EDR intervals, with several events showing sub-second differences. Among all detected candidates, three nulls satisfy strict numerical validity criteria, including a Type A null, a Type As null, and a Type Bs null.



***Corresponding Author:***

Sri Ekawati
Department of Computer Science, Graduate School of Science and Technology, University of Tsukuba
1-1-1 Tennodai, Tsukuba, Ibaraki 305-8573, Japan
Email: sri.ekawati@cavelab.cs.tsukuba.ac.jp

## 1. INTRODUCTION

One of the important problems in space plasma physics is how the solar wind interacts with the earth's magnetosphere [1], as illustrated in Figure 1. This interaction occurs at the magnetopause [2], [3], which is a complex boundary as a transition region between the solar wind and the earth's magnetosphere. The magnetopause is the boundary region where the solar wind, a continuous stream of charged particles from the Sun, interacts directly with the Earth's intrinsic magnetic field [4]-[6]. At the magnetopause, changes in the solar

wind pressure and interplanetary magnetic field orientation frequently trigger reconnection events, enabling solar wind plasma and energy to enter the magnetosphere [1], [6], [7]. These processes are closely linked to magnetospheric dynamics, including the onset of storms and substorms, which ultimately affect space weather near Earth. Magnetic reconnection is thought to originate and persist within a confined, electron-scale region called the electron diffusion region (EDR) [2], [3], [8], [9] where electrons become demagnetized [7], [10] uncoupled from the magnetic field [4]-[6]. In astrophysical plasma, such as the solar corona [11], coronal mass ejections [12], solar flare [13], stellar flares [14], and solar-terrestrial plasma, especially in magnetospheric substorms [15], [16], magnetic reconnection is a crucial process. Distinctive topological features naturally arise in magnetic reconnection regions, where the magnetic field strength vanishes [17], [18] the local magnetic topology becomes highly structured [19] commonly referred to as magnetic nulls [20]-[22]. As integral elements of reconnection geometry, magnetic null plays an important role in energy conversion and particle acceleration facilitating the breaking and rejoining of magnetic field lines into a new configuration [23], [24].

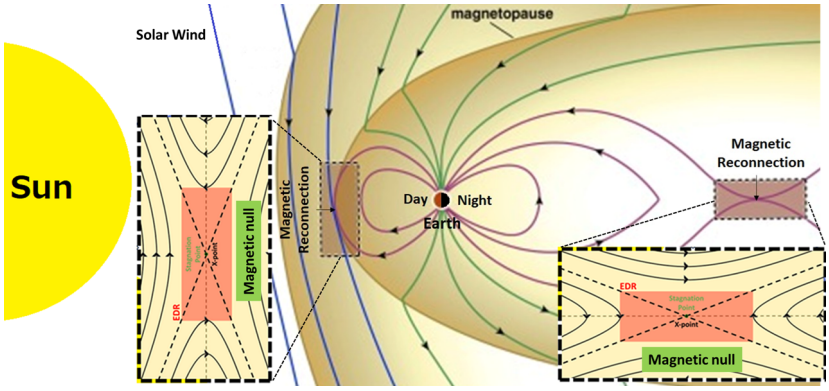


Figure 1. Illustration of the solar wind interaction with the Earth's magnetosphere, showing magnetic reconnection regions [4], [6] at the dayside magnetopause and nightside magnetotail

Magnetic nulls are theoretically well-defined, however, they remain practically challenging to locate, validate, and interpret within three-dimensional space plasma environments due to sensitivity to spacecraft geometry, numerical instability, and magnetic field fluctuations. Furthermore, magnetic nulls and the magnetic field topology surrounding the null also need visualization, as effective visualization plays a crucial role in interpreting complex, multidimensional scientific data [25], particularly in space plasma physics where magnetic topologies must be represented in three dimensions [26]. Accordingly, this study aims to develop an automated and reusable framework for magnetic null detection and visualization. Therefore, the main contributions of this framework are summarized as follows:

- An adaptive barycentric-based magnetic null detection algorithm that restricts localization to the nearest null within the multi-spacecraft tetrahedron,compared with existing approaches [1], [17], [27], [28], avoiding distant or extrapolated null candidates, improving geometric reliability and reducing false positives.
- A fully automated framework that eliminates manual parameter tuning required in previous studies [3].
- Physical validation criteria, including magnetic field reversal and explicit numerical criteria to ensure physically consistent solutions, were not implemented in previous studies [3].
- Three-dimensional visualization of the local magnetic topology applied to five events (the previous study [3] included only one event and no visualization).

## 2. PROPOSED COMPUTATIONAL FRAMEWORK

In this study, we introduce an adaptive null-detection method that automatically adjusts search parameters and incorporates magnetic field reversal validation and explicit numerical criteria, which have not been addressed in previous studies [3], enabling reuse across different events or datasets. In addition, three-dimensional visualization is integrated, and the overall workflow is shown in Figure 2. The framework is organized into two modular MATLAB components:

1 Null detection module [29], which performs temporal synchronization of the four-spacecraft data, ingests magnetic field and position measurements, detects magnetic null locations and times using barycentric interpolation with adaptive thresholds, validates field reversal, and stores the detected candidates.
2 Null classification and visualization module [30], which computes the magnetic gradient tensor $\nabla \mathbf{B}$, classifies null topology via eigenvalue analysis, applies numerical validation criteria, and generates three-dimensional visualizations of the local magnetic structure around each null.

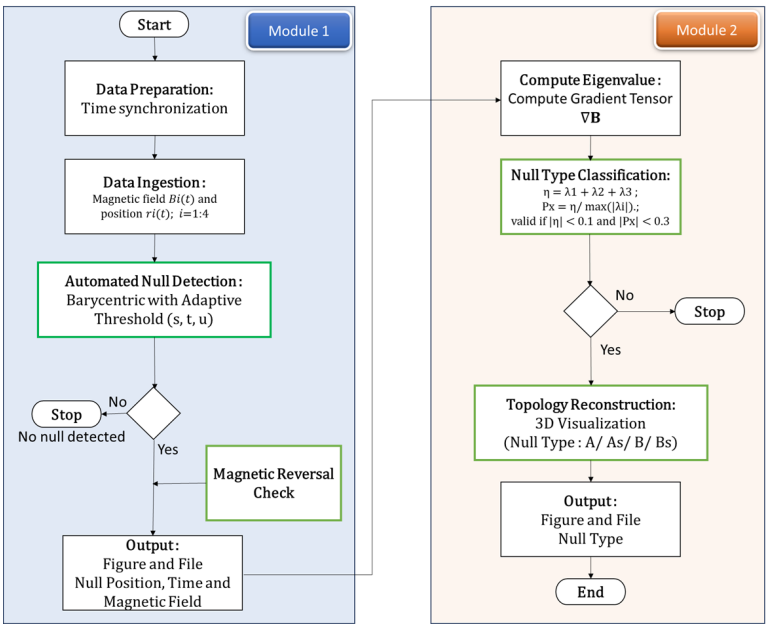


Figure 2. Flowchart of the proposed computational framework for automatic magnetic null detection, classification, and visualization

## 3. METHOD

### 3.1. Multi-spacecraft data

The framework leverages observations from NASA's magnetospheric multiscale (MMS) mission satellite, launched on March 12, 2015, which consists of four identically instrumented spacecraft flying in a tetrahedral formation. This configuration enables simultaneous measurements at four distinct spatial locations, providing the minimum requirements for reconstructing three-dimensional magnetic field gradients and accurately determining the position and topology of magnetic nulls. The MMS data provide publicly available high-resolution plasma and magnetic field measurements through the science data center (SDC) at `https://lasp.colorado.edu/mms/sdc/public/`. The MMS data are originally distributed in CDF format, however, the datasets used in this study were preprocessed and converted into MATLAB-ready ASCII files for efficient analysis. All processed datasets corresponding to the screened events are openly available on Zenodo [31].

This study analyzes five events: four previously reported EDR events (E1–E4)—E1 (2015-09-19 07:43:30 UTC) [2], [3], [9], E2 (2015-10-16 13:07:02 UTC) [2], [9], E3 (2015-10-22 06:05:22 UTC) [2], [9], and E4 (2017-08-10 12:18:33 UTC) [32], and one geomagnetic storm/substorm event (S1, 2017-05-28) [33]. In total, a substantially larger collection of MMS intervals was processed and screened using the proposed automated pipeline; however, only these five events [29] were detected.

### 3.2. Null detection

Before detecting magnetic null points, the converted ASCII files underwent additional preprocessing to ensure consistency across the four spacecraft. Temporal synchronization was applied to guarantee that all MMS data streams were aligned within a tolerance of $\epsilon = 0.001$ s, while timestamps were further adjusted to the UTC reference using cross-correlation with $\epsilon = 0.01$ s tolerance, and any non-overlapping intervals were

discarded. A custom MATLAB routine was developed to check synchronization, in which the detection time was considered valid only if all four spacecraft matched within 1 ms, with MMS1 serving as the reference clock. Data cleaning was also performed by removing invalid measurements, such that the cleaned dataset was formally defined as $D_{\text{clean}} = \{B_i, r_i \mid B_i \neq \text{NaN},\ r_i \neq \text{NaN}\}$, ensuring that only valid magnetic field vectors $B_i$ and spacecraft positions $r_i$ were retained for subsequent null detection analysis.

The automatic detection of magnetic null points was carried out using an adaptive threshold expansion method. The search was initialized with parameters $a = 0$, $b = 1$, and step size $\delta = 0.01$, and the boundaries were progressively expanded up to `max_expand` = 7, which allowed the algorithm to search beyond the initial MMS tetrahedron. At each iteration, the magnetic field vectors $\mathbf{B}_i$ and spacecraft positions $\mathbf{r}_i$ were extracted from the four MMS spacecraft. These relative magnetic field vectors were then employed to construct the matrix $\mathbf{A}$, which serves as the basis for estimating the null point location through a system of linear equations. The null is obtained by solving $\mathbf{A}[s,t,u]^T = -\mathbf{B}_1$, where $\mathbf{A} = [\mathbf{B}_2 - \mathbf{B}_1,\ \mathbf{B}_3 - \mathbf{B}_1,\ \mathbf{B}_4 - \mathbf{B}_1]^T$, using the approach previously reported in [3]. By solving this system for the coefficients $(s,t,u)$, the fourth barycentric coefficient is obtained as $d = 1 - s - t - u$. When the conditions $s,t,u \in [a,b]$ and $s + t + u \leq b$ are satisfied, the null position $\mathbf{r}_{\text{null}}$ can be determined as a weighted combination of the four spacecraft positions. Once a candidate null was found within the specified tolerance, its position and properties were recorded for further analysis.

After a candidate null point is detected, it undergoes a series of checks to confirm its physical and geometric plausibility. The magnetic field magnitudes $\|\mathbf{B}_i\|$ are evaluated for each MMS spacecraft and the signs of the $B_x$, $B_y$, and $B_z$ components are examined across all four spacecraft, as a valid null generally coincides with a reversal of the magnetic field in at least one component, indicating a true change in field direction. To assess the spatial configuration, the inter-satellite distances $d_{ij} = \|\mathbf{r}_i - \mathbf{r}_j\|$ and the distances from the null to each spacecraft $d_{\text{null-MMS}} = \|\mathbf{r}_i - \mathbf{r}_{\text{null}}\|$ are calculated, and the centroid of the tetrahedron is computed as $\mathbf{r}_{\text{centroid}} = \frac{1}{4}(\mathbf{r}_1 + \mathbf{r}_2 + \mathbf{r}_3 + \mathbf{r}_4)$ to ensure that the null lies reasonably within the observation volume.

### 3.3. Null classification

The detected candidate null is classified from the eigenvalues of the magnetic gradient tensor $\nabla\mathbf{B}$ [1], [3], [17], [19], [24], [34], enabling identification of radial or spiral three-dimensional topologies, as summarized in Table 1. At the detected candidate null, the local magnetic field is linearly approximated as $\mathbf{B}(\mathbf{r}) \approx \nabla\mathbf{B}(\mathbf{r} - \mathbf{r}_0)$, where the magnetic gradient tensor $\nabla\mathbf{B} \in \mathbb{R}^{3\times3}$ is obtained by solving a full $9\times9$ multi-point linear system constructed from the four MMS spacecraft measurements. The eigenvalues $\lambda_i = \text{eig}(\nabla\mathbf{B})$ are then computed to characterize the local topology. Physical consistency is enforced using the divergence-free constraint $\eta = \text{tr}(\nabla\mathbf{B}) = \lambda_1 + \lambda_2 + \lambda_3 \approx 0$ together with the normalized metric $p_x = |\eta|/(|\lambda_1| + |\lambda_2| + |\lambda_3|)$, and only solutions satisfying $|\eta| < \epsilon_1$ and $p_x < \epsilon_2$ are retained. The null type is subsequently determined from the eigenvalue signs: two negative and one positive eigenvalue indicate type A, two positive and one negative indicate type B, while the presence of a complex conjugate pair corresponds to spiral types (As/Bs).

Table 1. Classification of magnetic nulls based on eigenvalues of $\nabla\mathbf{B}$ [18], [34]

| $\lambda_1$ | $\lambda_2$ | $\lambda_3$ | Null type | Dimension/Structure | Labelling |
|---|---|---|---|---|---|
| 0 | $+\lambda$ | $-\lambda$ | X | 2-D | X |
| 0 | $+i\lambda$ | $-i\lambda$ | O | 2-D | ◯ |
| $-\lambda_1$ | $-\lambda_2$ | $+(\lambda_1+\lambda_2)$ | A | 3-D (radial) | △ |
| $+\lambda_1$ | $+\lambda_2$ | $-(\lambda_1+\lambda_2)$ | B | 3-D (radial) | ▽ |
| $+\lambda_1$ | $-\frac{\lambda_1}{2} + i\lambda_2$ | $-\frac{\lambda_1}{2} - i\lambda_2$ | As | 3-D (spiral) | ▲ |
| $-\lambda_1$ | $+\frac{\lambda_1}{2} + i\lambda_2$ | $+\frac{\lambda_1}{2} - i\lambda_2$ | Bs | 3-D (spiral) | ▼ |

### 3.4. Null visualization

The visualization of the magnetic topology is achieved through a 3D streamline plot generated around the null point. To characterize the local magnetic field structure, a first-order linear approximation is employed. Given the small spatial scales under consideration, the field is modeled as $\mathbf{B}_{\text{model}}(\mathbf{r}) = \nabla\mathbf{B} \cdot (\mathbf{r} - \mathbf{r}_{\text{null}})$, where $\nabla\mathbf{B}$ is the gradient tensor derived from the four MMS measurements and $\mathbf{r}$ denotes the position vector relative to the null. This reconstructed field is then evaluated on a regular 3D grid centered at $\mathbf{r}_{\text{null}}$, and the field lines are numerically integrated to produce the streamlines. In MATLAB, the streamlines are rendered together with the MMS tetrahedron and color-coded according to the null type, providing an intuitive representation of the local

3D magnetic structure. A regular 3D grid of seed points is constructed, typically forming a cube of side length $L$ centered at $\mathbf{r}_{\text{null}}$, where $L$ is proportional to the average inter-satellite distance of the MMS tetrahedron. The model field $\mathbf{B}_{\text{model}}(\mathbf{r})$ is computed at each grid point, and field lines are integrated numerically using standard streamline integration. In MATLAB, the visualization is performed by constructing a regular 3D grid centered at the null point, computing the local magnetic field at each grid point as $\mathbf{B}_{\text{local}} = \nabla\mathbf{B} \cdot (\mathbf{r} - \mathbf{r}_{\text{null}})$, coloring the field lines according to the null type, and overlaying the MMS tetrahedron to provide spatial context. Streamlines are integrated numerically to represent the local magnetic topology offering an intuitive depiction of the 3D field structure near each null. This visualization provides an intuitive representation of magnetic field lines near each null, facilitating the interpretation of local 3D magnetic structures.

## 4. RESULTS

The detection framework identified magnetic nulls in all five analyzed events. The computational characteristics for each event are summarized in Table 2. The number of iterations required for convergence varies across events. Event E1 (2015-09-19) converged after a single iteration using the initial search parameters $(a, b) = (0.00, 1.00)$. Event E2 (2015-10-16) and Event E3 (2015-10-22) required 71 and 150 iterations, respectively. Event E4 (2017-08-10) required 594 iterations. The special case S1 (2017-05-28) converged after 15 iterations with 365 synchronized time steps. The differences between the detected null times and the reported EDR intervals are less than one second for Events E1, E2, and E4, while Event E3 shows an offset of approximately six seconds. The detected null times for all events are listed in Table 2.

Table 2. Computational performance and null detection time compared with reported EDR intervals

| Event | Date | Iteration | Final (a,b) | Time steps | Null time (UTC) | EDR time (UTC) | Reference |
|---|---|---|---|---|---|---|---|
| E1 | 2015-09-19 | 1 | (0.00, 1.00) | 1999 | 07:43:30.840 | 07:43:30 | [2], [9] |
| E2 | 2015-10-16 | 71 | (-0.70, 1.70) | 4741 | 13:07:02.490 | 13:07:02 | [2], [9] |
| E3 | 2015-10-22 | 150 | (-1.49, 2.49) | 374 | 06:05:16.779 | 06:05:22 | [2], [9] |
| E4 | 2017-08-10 | 594 | (-5.93, 6.93) | 1112 | 12:18:33.423 | 12:18:32 | [32] |
| S1 | 2017-05-28 | 15 | (-0.15, 1.15) | 365 | 05:21:25.583 | – | Not reported |

The geometric characteristics of the detected nulls are summarized in Table 3. The MMS separation represents the characteristic size of the spacecraft tetrahedron, while the null–centroid distance and the normalized ratio $(d/R)$ describe the relative position of the null with respect to the formation. Event E1 exhibits barycentric coordinates within the range $0 < s, t, u < 1$, indicating that the null lies inside the tetrahedron. In contrast, E2 shows one negative parameter and a ratio close to unity, placing the null near the boundary. Events E3 and E4 show larger normalized distances and ratios exceeding one, indicating locations farther from the tetrahedron. The special case S1 yields a relatively small ratio ($\approx 0.37$) with one negative parameter, corresponding to a near-boundary position.

Table 3. Geometric parameters and relative position of detected nulls with respect to the MMS tetrahedron

| Event | Date | Parameter | | | MMS separation | Null–Centroid | Ratio | Location |
|---|---|---|---|---|---|---|---|---|
| | | $s$ | $t$ | $u$ | (km) | (km) | (d/R) | |
| E1 | 2015-09-19 | 0.051 | 0.625 | 0.306 | 71.662 | 28.892 | 0.40 | Inside |
| E2 | 2015-10-16 | 1.448 | 0.253 | -0.699 | 13.784 | 16.122 | 1.17 | Near |
| E3 | 2015-10-22 | 1.096 | 1.041 | 0.345 | 16.967 | 29.262 | 1.72 | Far |
| E4 | 2017-08-10 | 3.810 | -5.921 | 1.305 | 20.548 | 73.221 | 3.56 | Far |
| S1 | 2017-05-28 | 0.151 | 0.313 | -0.144 | 59.228 | 22.142 | 0.37 | Near |

Table 4 summarizes the average magnetic field magnitude and the reversal check across the three components for each event. Event E1 (2015-09-19) shows a relatively strong mean field of 25.249 nT with reversals detected in all three components. Event E2 (2015-10-16) exhibits a weaker mean field of 5.502 nT; no reversal is observed in $B_x$, while $B_y$ and $B_z$ display sign changes. Event E3 (2015-10-22) presents a stronger mean field of 22.246 nT with no reversal in any component. Event E4 (2017-08-10) is characterized by a weak mean field of 3.497 nT with a single reversal observed in $B_y$, while $B_x$ and $B_z$ remain monotonic. Finally, the special case S1 (2017-05-28) shows the lowest mean field of 0.859 nT with reversals present in all three components.

Table 4. Magnetic field statistics and reversal checks for each event

| Event | Date | Mean $\|B\|$ (nT) | $B_x$ Reversal | $B_y$ Reversal | $B_z$ Reversal |
|---|---|---|---|---|---|
| E1 | 2015-09-19 | 25.249 | Detected ([-1 1 -1 1]) | Detected ([-1 -1 -1 1]) | Detected ([-1 -1 -1 1]) |
| E2 | 2015-10-16 | 5.502 | No reversal ([-1 -1 -1 -1]) | Detected ([1 -1 -1 -1]) | Detected ([1 -1 -1 -1]) |
| E3 | 2015-10-22 | 22.246 | No reversal ([1 1 1 1]) | No reversal ([1 1 1 1]) | No reversal ([1 1 1 1]) |
| E4 | 2017-08-10 | 3.497 | No reversal ([1 1 1 1]) | Detected ([-1 1 1 1]) | No reversal ([-1 -1 -1 -1]) |
| S1 | 2017-05-28 | 0.859 | Detected ([-1 -1 1 -1]) | Detected ([-1 -1 1 1]) | Detected ([1 -1 -1 -1]) |

Table 5 summarizes the classification outcomes of the detected nulls for the five analyzed events (E1–E4 and S1). Three events (E1, E2, and S1) satisfy the validation criteria and are classified as valid nulls, while the remaining two events (E3 and E4) exceed the prescribed thresholds and are therefore classified as invalid. Among the validated cases, both radial and spiral topologies are observed, indicating variability in the local magnetic field structure across events.

Table 5. Eigenvalues of $\nabla \mathbf{B}$ at detected nulls, validated via the $\eta = \lambda_1 + \lambda_2 + \lambda_3$ and $P_x = \eta / \max(|\lambda_i|)$. Nulls are considered valid if $|\eta| < 0.1$ and $|P_x| < 0.3$, and classified according to Table 1

| Event | Date | $\lambda_1$ | $\lambda_2$ | $\lambda_3$ | $\eta$ | $P_x$ | Validity | Type |
|---|---|---|---|---|---|---|---|---|
| E1 | 2015-09-19 | 0.5444 | -0.3736 | -0.2040 | -0.0338 | -0.0621 | Valid | A |
| E2 | 2015-10-16 | -0.0415+0.4185i | -0.0415-0.4185i | 0.1782 | 0.0952 | 0.2265 | Valid | As |
| E3 | 2015-12-05 | -0.4953 | 0.1092 | 0.1906 | -0.1956 | -0.3948 | Invalid | - |
| E4 | 2017-08-10 | -0.0253 | 0.0246 | 0.0135 | 0.0128 | 0.5049 | Invalid | - |
| S1 | 2017-05-28 | -0.0173+0.0000i | 0.0066+0.0124i | 0.0066-0.0124i | -0.0041 | -0.2381 | Valid | Bs |

Figure 3 presents three-dimensional reconstructions of the magnetic field topology surrounding the detected nulls for representative events. Figure 3(a) shows Event E1 (2015-09-19), a Type A null, featuring a clear radial configuration with field lines diverging along one principal direction and converging along the others. Figure 3(b) illustrates Event E2 (2015-10-16), a Type As null, where the field exhibits a distinct spiral pattern indicative of rotational topology. Figure 3(c) depicts Event S1 (2017-05-28), a Type Bs null, also displaying a spiral structure consistent with its eigenvalue-based classification. These three-dimensional visualizations faithfully reproduce the geometrical differences between radial and spiral nulls, providing direct, visual confirmation of the classifications reported in Tables 3-5. The reconstructed field lines, computed from the locally linearized magnetic field, convincingly highlight the topological signatures unique to each null type.

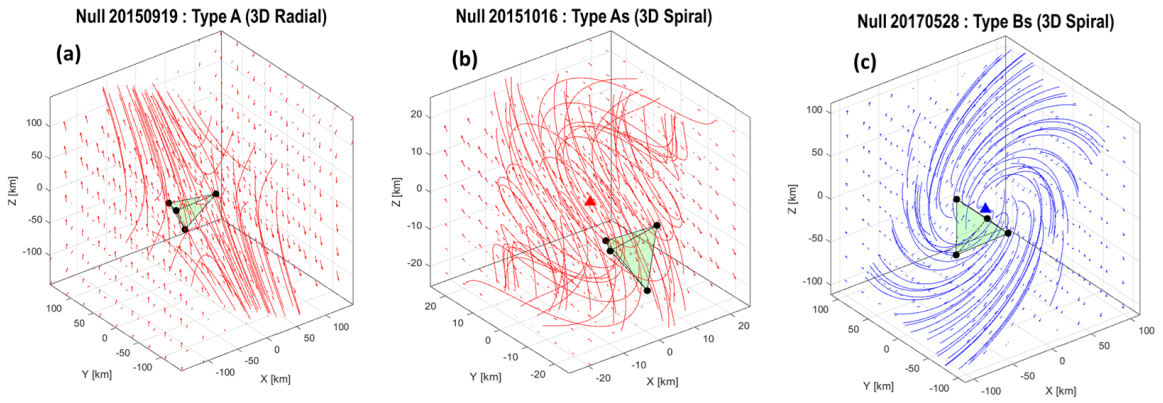


Figure 3. Three-dimensional reconstructions of magnetic field topology around detected nulls: (a) Type A (radial, E1), (b) Type As (spiral, E2), and (c) Type Bs (spiral, S1). Field lines are computed from the locally linearized magnetic field and illustrate the distinct topological structures associated with each null type

## 5. DISCUSSION

The detected null times closely match the reported EDR intervals, often within sub-second differences (Events E1 and E2 shown in Tables 2), demonstrating temporal accuracy and confirming that the identified nulls represent physically meaningful reconnection structures rather than numerical artifacts. Differences in iteration counts primarily reflect the relative position of the null with respect to the spacecraft tetrahedron rather than numerical instability: interior nulls converge rapidly (Event E1), whereas more distant nulls require substantially more iterations (Event E4), indicating a computationally more demanding search. Nulls located inside or near the tetrahedron are generally better constrained by the four-point measurements and therefore more robustly defined (e.g., E1, E2 and S1 shown in Tables 3), whereas distant nulls (e.g., E3 and E4 shown in Tables 3) are more sensitive to interpolation errors and gradient uncertainties.

Magnetic field reversals provide an important physical validation of the detected nulls. Events with reversals in all or at least two components (E1, E2, and S1 in Table 4) are consistent with true null structures, whereas partial or absent reversals (E3–E4) indicate weaker or less reliable candidates. Importantly, the presence of magnetic field reversals across multiple components provides a more reliable physical signature of a true null than the absolute field magnitude.

The Eigenvalue analysis of the gradient tensor $\nabla \mathbf{B}$ further elucidates the local magnetic topology. Radial and spiral configurations observed in Events E1, E2, and S1 agree with theoretical expectations for three-dimensional nulls associated with reconnection. In contrast, invalid classifications in Events E3 and E4 likely arise from asymmetric gradients or increased uncertainty when the null is located far from the spacecraft, highlighting a practical limitation of linear interpolation methods, namely that the accuracy of $\nabla \mathbf{B}$ decreases with extrapolation distance. Combining geometric constraints with eigenvalue validation is therefore essential to minimize false positives.

These geometric indicators, together with magnetic field reversal and eigenvalue analyses, provide comprehensive validation of each detection. Figure 3 further confirms the results through three-dimensional topology reconstructions, where Event E1 shows a radial Type A null, while Events E2 and S1 exhibit spiral Type As/Bs structures. The reconstructed field lines, obtained from the locally linearized magnetic field, clearly differentiate radial and spiral topologies and visually confirm the classifications reported in Tables 3–5. Overall, the agreement between geometric, physical, eigenvalue, and visual analyses, together with the clear separation between radial and spiral patterns, visually supports the classifications and reinforces the robustness of the proposed framework.

## 6. CONCLUSION

Combining adaptive numerical search, geometric validation, and physical topology analysis provides a reliable, computationally efficient strategy for automatic magnetic null detection in multi-spacecraft observations. The framework consistently distinguishes well-constrained nulls from distant or ambiguous candidates, robustly characterizes local topology, and offers practical utility for reconnection studies. Across all investigated events, the framework consistently detected candidate nulls with timings closely aligned with reported reconnection and EDR intervals, demonstrating both numerical robustness and physical consistency. Geometric and topological validations further distinguished well-constrained nulls located inside or near the MMS tetrahedron from marginal candidates at larger distances, while eigenvalue analysis enabled systematic classification into radial and spiral types. These results show that the proposed approach provides not only accurate localization but also meaningful physical interpretation of the three-dimensional magnetic topology. In summary, the framework offers an efficient and scalable tool for automated magnetic null detection in multi-spacecraft observations.

Future work will focus on integrating direct ingestion of MMS CDF files into the MATLAB pipeline, applying the framework to additional datasets, implementing Earth Mover's Distance (EMD)-based methods, and extending the framework toward multi-null detection using higher-order polynomial interpolation.

## ACKNOWLEDGMENTS

The authors thank the MMS (Magnetospheric Multiscale) mission team for providing the data. The authors also thank anonymous reviewers for their constructive comments.

**FUNDING INFORMATION**

Authors state no funding involved.

**AUTHOR CONTRIBUTIONS STATEMENT**

This journal uses the Contributor Roles Taxonomy (CRediT) to recognize individual author contributions, reduce authorship disputes, and facilitate collaboration.

| Name of Author | C | M | So | Va | Fo | I | R | D | O | E | Vi | Su | P | Fu |
|---|---|---|---|---|---|---|---|---|---|---|---|---|---|---|
| Sri Ekawati | ✓ | ✓ | ✓ | ✓ | ✓ | ✓ | ✓ | ✓ | ✓ | ✓ | ✓ | | ✓ | |
| Dongsheng Cai | ✓ | ✓ | | | ✓ | | ✓ | | | | | ✓ | ✓ | |
| Hiroyuki Kudo | | | | | | | ✓ | | | | | ✓ | ✓ | |

C : **C**onceptualization
M : **M**ethodology
So : **So**ftware
Va : **Va**lidation
Fo : **Fo**rmal Analysis
I : **I**nvestigation
R : **R**esources
D : **D**ata Curation
O : Writing - **O**riginal Draft
E : Writing - Review & **E**diting
Vi : **Vi**sualization
Su : **Su**pervision
P : **P**roject Administration
Fu : **Fu**nding Acquisition

**CONFLICT OF INTEREST STATEMENT**

Authors state no conflict of interest.

**DATA AVAILABILITY**

The preprocessed datasets corresponding to the five analyzed events are openly available on Zenodo at `https://doi.org/10.5281/zenodo.16070912`, and all preprocessed MMS datasets associated with the screened intervals used for magnetic null detection are openly available at `https://zenodo.org/records/18437216`. The original high-resolution data are publicly accessible through the Magnetospheric Multiscale (MMS) mission Science Data Center (SDC) at `https://lasp.colorado.edu/mms/sdc/public/`.

**REFERENCES**

[1] E. Eriksson, A. Vaivads, Y. V. Khotyaintsev, V. M. Khotyayintsev, and M. André, "Statistics and accuracy of magnetic null identification in multispacecraft data," *Geophysical Research Letters*, vol. 42, no. 17, pp. 6883–6889, Sep. 2015, doi: 10.1002/2015GL064959.

[2] J. M. Webster *et al.*, "Magnetospheric multiscale dayside reconnection electron diffusion region events," *Journal of Geophysical Research: Space Physics*, vol. 123, no. 6, pp. 4858–4878, Jun. 2018, doi: 10.1029/2018JA025245.

[3] S. Ekawati and D. Cai, "In-situ observation of magnetic null on 19 September 2015 event using magnetospheric multiscale mission," *Journal of Geophysical Research: Space Physics*, vol. 128, no. 2, Feb. 2023, doi: 10.1029/2021JA029571.

[4] J. L. Burch, T. E. Moore, R. B. Torbert, and B. L. Giles, "Magnetospheric multiscale overview and science objectives," *Space Science Reviews*, vol. 199, no. 1–4, pp. 5–21, Mar. 2016, doi: 10.1007/s11214-015-0164-9.

[5] J. L. Burch *et al.*, "Electron-scale measurements of magnetic reconnection in space," *Science*, vol. 352, no. 6290, Jun. 2016, doi: 10.1126/science.aaf2939.

[6] Q. Lenouvel *et al.*, "Identification of electron diffusion regions with a machine learning approach on MMS data at the earth's magnetopause," *Earth and Space Science*, vol. 8, no. 5, May 2021, doi: 10.1029/2020EA001530.

[7] J. L. Burch and T. D. Phan, "Magnetic reconnection at the dayside magnetopause: Advances with MMS," *Geophysical Research Letters*, vol. 43, no. 16, pp. 8327–8338, Aug. 2016, doi: 10.1002/2016GL069787.

[8] S. A. Fuselier and W. S. Lewis, "Properties of near-earth magnetic reconnection from in-situ observations," *Space Science Reviews*, vol. 160, no. 1–4, pp. 95–121, Oct. 2011, doi: 10.1007/s11214-011-9820-x.

[9] S. A. Fuselier *et al.*, "Large-scale characteristics of reconnection diffusion regions and associated magnetopause crossings observed by MMS," *Journal of Geophysical Research: Space Physics*, vol. 122, no. 5, pp. 5466–5486, May 2017, doi: 10.1002/2017JA024024.

[10] T. D. Phan *et al.*, "Electron magnetic reconnection without ion coupling in Earth's turbulent magnetosheath," *Nature*, vol. 557, no. 7704, pp. 202–206, May 2018, doi: 10.1038/s41586-018-0091-5.

[11] M. S. Freed, D. W. Longcope, and D. E. McKenzie, "Three-year global survey of coronal null points from potential-field-source-surface (PFSS) modeling and solar dynamics observatory (SDO) observations," *Solar Physics*, vol. 290, no. 2, pp. 467–490, Feb. 2015, doi: 10.1007/s11207-014-0616-5.

[12] J. Lin and T. G. Forbes, "Effects of reconnection on the coronal mass ejection process," *Journal of Geophysical Research: Space Physics*, vol. 105, no. A2, pp. 2375–2392, Feb. 2000, doi: 10.1029/1999JA900477.
[13] P. Demoulin, J. C. Henoux, and C. H. Mandrini, "Are magnetic null points important in solar flares?," *Astronomy and Astrophysics*, vol. 285, no. 1, pp. 1023–1037, 1994.
[14] K. Shibata, *et al.*, "Hot-plasma ejections associated with compact-loop solar flares," *The Astrophysical Journal*, vol. 451, no. 2, 1995, doi: 10.1086/309688.
[15] V. Angelopoulos *et al.*, "Tail reconnection triggering substorm onset," *Science*, vol. 321, no. 5891, pp. 931–935, Aug. 2008, doi: 10.1126/science.1160495.
[16] T. Nagai *et al.*, "Structure and dynamics of magnetic reconnection for substorm onsets with Geotail observations," *Journal of Geophysical Research: Space Physics*, vol. 103, no. A3, pp. 4419–4440, 1998, doi: 10.1029/97ja02190.
[17] H. S. Fu *et al.*, "How to find magnetic nulls and reconstruct field topology with MMS data?," *Journal of Geophysical Research: Space Physics*, vol. 120, no. 5, pp. 3758–3782, 2015, doi: 10.1002/2015JA021082.
[18] H. S. Fu *et al.*, "Evidence of magnetic nulls in electron diffusion region," *Geophysical Research Letters*, vol. 46, no. 1, pp. 48–54, Jan. 2019, doi: 10.1029/2018GL080449.
[19] C. J. Xiao *et al.*, "In situ evidence for the structure of the magnetic null in a 3D reconnection event in the Earth's magnetotail," *Nature Physics*, vol. 2, no. 7, pp. 478–483, Jul. 2006, doi: 10.1038/nphys342.
[20] R. G. Glovanelli, "A theory of chromospheric flares," *Nature*, vol. 158, no. 4003, pp. 81–82, Jul. 1946, doi: 10.1038/158081a0.
[21] J. Dungey, *Cosmic Electrodynamics*. Cambridge University Press, 1958.
[22] R. Guo, Z. Pu, X. Wang, C. Xiao, and J. He, "3D reconnection geometries with magnetic nulls: multispacecraft observations and reconstructions," *Journal of Geophysical Research: Space Physics*, vol. 127, no. 2, Feb. 2022, doi: 10.1029/2021JA030248.
[23] X. H. Chen *et al.*, "Magnetic Nulls in the Reconnection Driven by Turbulence," *The Astrophysical Journal*, vol. 852, no. 1, p. 17, Jan. 2018, doi: 10.3847/1538-4357/aa9991.
[24] C. J. Xiao *et al.*, "Satellite observations of separator-line geometry of three-dimensional magnetic reconnection," *Nature Physics*, vol. 3, no. 9, pp. 609–613, Sep. 2007, doi: 10.1038/nphys650.
[25] K. G. Preetha, S. Saritha, J. Jeevan, C. Sachidanandan, and P. A. Maheswaran, "An interactive visualization tool for the exploration and analysis of multivariate ocean data," *Indonesian Journal of Electrical Engineering and Computer Science (IJEECS)*, vol. 36, no. 2, pp. 1329–1337, 2024, doi: 10.11591/ijeecs.v36.i2.pp1329-1337.
[26] P. Xiong, S. Fujita, M. Watanabe, T. Tanaka, and D. Cai, "Identifying and visualizing terrestrial magnetospheric topology using geodesic level set method," *Computer Graphics Forum*, vol. 43, no. 1, Feb. 2024, doi: 10.1111/cgf.14994.
[27] P. Developer, "PySPEDAS: space physics environment data analysis software in python." [Online]. Available: https://pyspedas.readthedocs.io
[28] P. Developers, "Pyspedas: magnetic null finding tools." [Online]. Available: https://pyspedas.readthedocs.io
[29] S. Ekawati, "MMS null detection and data processing pipeline [MATLAB code]," Zenodo, 2025, doi: 10.5281/zenodo.16070912.
[30] S. Ekawati, "MMS null topology classification and visualization suite [MATLAB code]," *Zenodo*, 2025, [Online]. Available: https://doi.org/10.5281/zenodo.16070912
[31] S. Ekawati, "Preprocessed MMS dataset for magnetic null detection," *Zenodo*, 2026.
[32] M. Zhou *et al.*, "Observations of an electron diffusion region in symmetric reconnection with weak guide field," *The Astrophysical Journal*, vol. 870, no. 1, p. 34, Jan. 2019, doi: 10.3847/1538-4357/aaf16f.
[33] T. Sori, A. Shinbori, Y. Otsuka, M. Nishioka, S. Perwitasari, and N. Nishitani, "First detection of midlatitude plasma bubble by SuperDARN during a geomagnetic storm on May 27 and 28, 2017," *Journal of Geophysical Research: Space Physics*, vol. 128, no. 4, Apr. 2023, doi: 10.1029/2022JA031157.
[34] Y.-T. Lau and J. M. Finn, "Three-dimensional kinematic reconnection in the presence of field nulls and closed field lines," *The Astrophysical Journal*, vol. 350, p. 672, Feb. 1990, doi: 10.1086/168419.

## BIOGRAPHIES OF AUTHORS

**Sri Ekawati** is currently a researcher at the Research Center for Climate and Atmosphere, Indonesia's National Research and Innovation Agency (BRIN), and a Ph.D. student in the Department of Computer Science at the University of Tsukuba, Japan. She received her B.Sc. degree in Physics from Universitas Padjadjaran, Indonesia (2005), and her M.Sc. degree from Institut Teknologi Bandung, Indonesia (2014). Since 2006, she has been with the Indonesian National Institute of Aeronautics and Space (LAPAN), which was later integrated into BRIN in 2021, where her research has focused on space weather, particularly magnetospheric and ionospheric physics. For this paper, she led the research design, developed the computational programs, and prepared the manuscript. She can be contacted at email: sri.ekawati@cavelab.cs.tsukuba.ac.jp or sri.ekawati@brin.go.id.

**Dongsheng Cai** was a professor in the Department of Computer Science at the University of Tsukuba, Japan. He is currently a Professor of Management at the Nagoya University of Commerce and Business (NUCB), Japan, and received his Ph.D. degree from Stanford University, USA. His research interests include high-performance computing, artificial intelligence, quantum computing, data science, and space physics simulations. For this paper, he contributed to the conceptualization of the study, provided guidance on the initial methodology, supervised the research, and supplied the data used. He can be contacted at email: cai@cs.tsukuba.ac.jp.

**Hiroyuki Kudo** is a professor in the Department of Computer Science at the University of Tsukuba, Japan. He received his Doctor of Engineering degree in Electrical and Communication Engineering from Tohoku University, Japan, in March 1990. His research interests include intelligent informatics, biomedical engineering, biomaterials, and medical imaging systems. For this paper, he provided supervision, access to essential resources throughout the study, and manuscript refinement. He can be contacted at email: kudo@cs.tsukuba.ac.jp.